

1

2 **Use of A High-Resolution-Satellite-Based Precipitation Product in**  
3 **Mapping Continental-Scale Rainfall Erosivity:**  
4 **A Case Study of the United States**

5

6 Jungho Kim<sup>a,b</sup>, Heechan Han<sup>c</sup>, Boran Kim<sup>c</sup>,

7 Haonan Chen<sup>a,b</sup>, Jai-Hong Lee<sup>d</sup>

8

9 <sup>a</sup> Cooperative Institute for Research in the Atmosphere (CIRA), Colorado State University,  
10 Fort Collins, Colorado, U.S.A.

11 <sup>b</sup> NOAA Earth System Research Laboratory, Physical Sciences Division, Boulder, Colorado,  
12 U.S.A.

13 <sup>c</sup> Department of Civil and Environmental Engineering, Colorado State University, Fort  
14 Collins, Colorado, U.S.A.

15 <sup>d</sup> Department of Civil and Mechanical Engineering, South Carolina State University,  
16 Orangeburg, SC, U.S.A.

17

18

19 Corresponding author: Heechan Han (postal address: Department of Civil and Environmental  
20 Engineering, Colorado State University, Fort Collins, 80523, Colorado, U.S.A.; e-mail:  
21 heechan.han@colostate.edu)

22

23 Submitted to *Catena*

24

25

26

27

## Abstract

28

29 A rainfall erosivity map is useful for understanding the spatial variability of rainfall erosivity,  
30 and for identifying regions vulnerable to soil erosion by rainfall. This study addresses a new  
31 approach to mapping rainfall erosivity on a continental scale, based on a high-resolution-  
32 satellite-based precipitation product—the National Oceanic and Atmospheric and  
33 Atmospheric Administration’s Climate Precipitation Center morphing technique (CMORPH).  
34 For this purpose, a rainfall erosivity map of the contiguous United States is experimentally  
35 developed, and is analyzed from the perspectives of the corresponding hydrological basins  
36 and climate features. In general, we conclude that the CMORPH precipitation product is  
37 useful for mapping rainfall erosivity on a continental scale. In the contiguous United States,  
38 the mean of rainfall erosivity was  $1,260 \text{ MJ mm ha}^{-1} \text{ h}^{-1} \text{ yr}^{-1}$ , with high variability by region.  
39 The coastal regions showed the highest rainfall erosivity, at 20%. The seasonality of the  
40 rainfall erosivity was evident in most coastal regions (rainfall erosivity depends on climates).  
41 The rainfall erosivity in the tropical climate zone was the highest, whereas it was the lowest  
42 in the arid climate zone (and spatially homogeneous). However, corrections were required for  
43 improving the accuracy of the CMORPH precipitation in most coastal regions, i.e., to secure  
44 a better rainfall erosivity product. Compared to a rain gauge-based rainfall erosivity map, the  
45 CMORPH’s rainfall erosivity map tended to underestimate the rainfall erosivity in coastal  
46 regions near the Gulf of Mexico and Atlantic Ocean, but overestimated it in coastal regions  
47 near the Pacific Ocean.

48

49 **Keywords:** Soil erosion; Rainfall erosivity; R-factor; High resolution satellite-based  
50 precipitation; CMORPH

51     **1. Introduction**

52

53         The identification of regions vulnerable to soil erosion is very important, as soil loss  
54         has a significant influence on reductions in agricultural land, reservoir capacity, water quality,  
55         and carbon sequestration (Conner et al., 1989; Smith et al., 2001; Lal, 2005; Panagos et al.,  
56         2016a; 2016b). Typically, soil erosion (e.g., interrill erosion) is caused by two physical  
57         processes (Nearing et al., 1994): a soil particle separation process owing to the impact of the  
58         rainfall kinetic energy on the soil surface, and a sediment transportation process owing to  
59         surface flows. The erosion depends on the rainfall features in the region (e.g., intensity and  
60         terminal velocity), as well as the topographical and pedological features (e.g., slope, soil type,  
61         and vegetative cover) (Jayawardena and Rezaur, 2000). The rainfall intensity and its kinetic  
62         energy on the soil surface are the primary factors causing interrill erosion, as these factors  
63         lead to the physical separation of soil particles. In the hydrologic community, the rainfall  
64         erosion index (a R-factor based on the two factors) has been used to quantitatively represent  
65         and measure degrees of soil erosion from rainfall (Goovaerts, 1999; Panagos et al., 2016a).  
66         The universal soil loss equation (USLE, Wischmeier and Smith, 1978) and revised USLE  
67         (Renard et al., 1991) are good examples of calculations that employ the R-factor as a major  
68         parameter in estimating soil loss. However, it is challenging to map rainfall erosivity using  
69         ground-based rain-gauge observations (hereinafter referred to rain-gauge data), as they  
70         cannot represent the spatial distribution of the precipitation. As such, they require  
71         interpolation to map the rainfall erosivity. Accordingly, high-resolution-satellite-based  
72         precipitation products might be an alternative to mapping rainfall erosivity on a large scale.

73         The R-factor has been estimated using various methods dependent on various  
74         temporal resolutions of precipitation data: sub-hourly (Wischmeier and Smith, 1978; Yin et  
75         al., 2007), hourly (Ramos and Durán, 2014), daily (Angulo-Martínez and Beguería, 2009),

76 monthly (Renard and Freimund, 1994; Hernando and Romana, 2015), and yearly (Lee and  
77 Heo, 2011) data. The point-scale R-factor estimated from these methods has been mapped  
78 using an interpolation approach, allowing researchers to estimate amounts of potential rainfall  
79 erosivity in ungauged areas, understand the spatial variability, and identify regions vulnerable  
80 to soil erosion. As a result, over the last four decades, rainfall erosivity maps have been  
81 presented on various scales: continental-scale maps (Roose, 1977; Oduro-Afriyie, 1998;  
82 Panagos et al., 2015), national-scale maps (Elwell and Stocking, 1976; Krauer, 1988; Lenvain  
83 et al., 1988; Oduro-Afriyie, 1996; Mikhailova et al., 1997; Da Silva, 2004; Leow et al., 2011;  
84 Klik et al., 2015; Panagos et al., 2016a), and regional-scale maps (Angulo-Martinez and  
85 Beguería, 2009; Ufoegbune et al., 2011; Elbasit et al., 2013; Ramos and Durán, 2014).  
86 Panagos et al. (2017) developed a novel global R-factor map for representing high spatial  
87 variability in rainfall erosivity for six continents, using rain-gauge data collected from 63  
88 countries.

89 The first rainfall erosivity map in the United States was introduced in an agriculture  
90 handbook (Wischmeier and Smith, 1965). The map was developed from 22 years of rainfall  
91 records, and 11 of the western states were omitted from the map, as sufficient long-term  
92 recording-rain-gauge records were unavailable. In 1997, the United States Department of  
93 Agriculture revised the map, using rainfall records from 1,082 stations over 20 years (Renard  
94 et al., 1997). The rainfall erosivity map was divided into five regions: Eastern and Western  
95 United States, California, Oregon, and Washington, and Hawaii. Since then, only a few  
96 studies have developed soil erosivity maps for the United States (Niedermeier, 1998; Wang et  
97 al., 2002; Cooper, 2011).

98 Using rain-gauge data to estimate the R-factor is the easiest way to secure and handle  
99 data. However, many studies addressed the limitations in employing rain-gauge data  
100 compared to remote sensing data, such as the advantages of satellite-based precipitation

101 products in being able to capture the spatial distribution of precipitation regardless of the type  
102 of terrain, and the ability to track a storm from the ocean to an inland area (Buytaert et al.,  
103 2006; Nesbitt and Anders, 2009; Anagnostou et al., 2010; Kim and Yoo, 2014; Kim et al.,  
104 2015). Technically, the rain-gauge data can only represent a measured value within a  
105 constrained radius of observation instruments, as it is a point-scale. In addition, it is affected  
106 by the sampling density of rain-gauge data, which can vary with different terrain types. Thus,  
107 the greatest uncertainty in the rainfall erosivity map constructed from rain-gauge data is  
108 probably related to the transition areas between different topographic conditions, climate  
109 zones, and ungauged areas (Panagos et al., 2017).

110 Most studies using rain-gauge data have employed a spatial interpolation method for  
111 predicting and mapping rainfall erosivity in the transition areas, e.g., inverse distance  
112 weighting, radial basis functions, regression, kriging, and co-kriging methods (Goovaerts,  
113 1999; LOWLAND, 2005; Bonilla and Vidal, 2011; Khorsandi et al., 2012; Meusburger et al.,  
114 2012; Lee and Lin, 2015; Meddi et al., 2016). Thus, there is a high possibility that the  
115 interpolated rainfall erosivity values will have a large amount of uncertainty, arising from the  
116 use of an interpolation method (Goovaerts, 1999; Panagos et al., 2015; Ballabio et al., 2017).  
117 Vrieling et al. (2010) and Zhu et al. (2011), understood the usefulness of remote sensing data,  
118 and utilized 3-hourly satellite-based precipitation data (e.g., tropical rainfall measuring  
119 mission products, (TRMM)) to map rainfall erosivity. Vrieling et al. (2010) concluded that  
120 the 3-hourly and 0.25° (approximately 27 km temporal resolution) resolutions of the TRMM  
121 data provided insufficient details for representing high-intensity erosive events. Zhu et al.  
122 (2011) indicated that the 3-hourly temporal resolution was not sufficiently fine to map  
123 rainfall erosivity, and recommended a sub-hourly temporal resolution for mapping. These  
124 conclusions have consistently provided support for employing high-resolution-satellite-based

125 precipitation products with a sub-hourly temporal resolution to estimate and map rainfall  
126 erosivity on a continental scale.

127 This study aims to propose a new approach for estimating and mapping a rainfall  
128 erosivity index, the R-factor, on a continental scale. The approach employs a high-resolution-  
129 satellite-based precipitation product, i.e., the National Oceanic and Atmospheric  
130 Administration (NOAA) Climate Precipitation Center morphing technique precipitation  
131 product (hereinafter referred to CMORPH). In addition, the approach employs a standard  
132 method that requires precipitation data in a 30-min temporal resolution. As a case study, the  
133 approach is applied to the contiguous United States (CONUS). The rainfall erosivity map  
134 over the CONUS is analyzed to identify and understand the rainfall erosivity attributes from  
135 various points of view: annual, monthly, hydrologic unit basins, and climate zones.

136

## 137 **2. Materials and Methods**

138

### 139 **2.1 Study Area**

140

141 The CONUS is chosen as the application domain because it has a variety of  
142 geographic and climate features. The CONUS consists of the 48 states of the US (excluding  
143 Alaska, Hawaii, and the Caribbean) and eighteen river basins, based on the United States  
144 Geological Survey hydrologic unit codes. These basins include either the drainage area of a  
145 major river, or the combined drainage areas of a series of rivers (Seaber et al. 1987, Ahn, K.  
146 H., Palmer). The climate features of the CONUS vary owing to the impacts of oceans (e.g.,  
147 the Pacific Ocean, Gulf of Mexico, and Atlantic Ocean) and geographic features, including  
148 mountains and arid/semi-arid deserts. It consists of 15 climate zones such as tropical, arid,

149 temperate, and cold. Generally, the climate of the CONUS becomes warm and dry in the west  
150 and south regions, and humid in the east and north regions.

151 The annual precipitation over the CONUS is approximately 760 mm, and varies with  
152 regional topography and climate characteristics. For example, for western regions with warm  
153 and dry climatic features, the average annual precipitation is approximately 630 mm, whereas  
154 it is approximately 1,250 mm for southeastern regions. In addition, the average annual  
155 precipitation in the central regions unaffected by oceans is approximately 420 mm, which is  
156 relatively lower than the other regions.

157 Unlike the central regions, precipitation in the western and southeastern regions is  
158 affected by the oceans. In the western region, extratropical cyclones or jet streams (usually  
159 from the Pacific Ocean between September and May) cause a large amount of rainfall  
160 ([https://www.wpc.ncep.noaa.gov/research/mcs\\_web\\_test\\_test\\_files/Page1539.htm](https://www.wpc.ncep.noaa.gov/research/mcs_web_test_test_files/Page1539.htm)).

161 Moreover, atmospheric rivers cause heavy rainfall during the rainy season (Ralph et al., 2006;  
162 Han et al., 2019). The southeastern regions have higher amounts of precipitation than the  
163 other regions, mainly owing to the humid air coming from the Atlantic and Caribbean Oceans  
164 and the Gulf of Mexico. Between late summer and early fall, tropical cyclones move from the  
165 Atlantic Ocean and Gulf of Mexico to the southeastern regions, providing a quarter of the  
166 annual precipitation (Knight and Davis, 2007).

167

168

169 **2.2 CMORPH Precipitation Product**

170

171 The CMORPH is a very high spatial and temporal resolution global precipitation  
172 product that covers over the CONUS, with a history longer than ground-based remote sensing  
173 data such as weather radars. The CMORPH produces global precipitation estimates at an 8

174 km × 8 km resolution every 30 min. Overall, this technique exclusively uses precipitation  
175 estimates derived from low Earth orbit (LEO) satellite-derived passive microwave (PMW)  
176 observations. As the coverage of the PMW-based retrievals is severely limited in the half-  
177 hour window owing to the spatial and temporal sampling natures of LEO satellites (even  
178 when multiple satellites are used), the CMORPH takes advantage of the high temporal  
179 resolution of the geostationary satellite infrared (IR) imagery to create motion vectors for the  
180 cloud systems. It subsequently applies the cloud motion vectors to the available PMW-based  
181 retrievals to produce continuous precipitation estimates over the entire globe. At each half-  
182 hour window, the availability of the IR data is almost guaranteed at a given location, and can  
183 be used to extract the spatial propagation of precipitation features. For additional details  
184 regarding the CMORPH technique, interested readers are referred to Joyce et al. (2004), Xie  
185 et al. (2017) and Chen et al. (2020).

186 The entire CMORPH dataset in version 1.0 is reprocessed and extended to cover the  
187 period from 1998 to the present. The reprocessing includes a bias correction using gauge data  
188 (Xie et al. 2017). There are three types of precipitation estimates from the CMORPH: 30-  
189 min/8 km, 3-h/0.25°, and 1-day/0.25°. As the CMORPH provides precipitation data over 30  
190 min in mm/h, to obtain hourly precipitation estimates for calculating the R-factor, each half-  
191 hourly rainfall rate estimate is assumed to be constant for the entire half hour (e.g., a 1.0  
192 mm/h rainfall rate estimate over 30 min = 0.5 mm of accumulated precipitation during that  
193 time). Each 30-min estimate is accumulated to obtain the hourly precipitation.

194 This study is conducted with the understanding that the accuracy of the CMORPH  
195 might be lower than that of rain-gauge data in some regions, and briefly compares the  
196 CMORPH precipitation data with the rain-gauge data in the discussion part.

197

198 **2.3 Rainfall Erosivity Index: R-factor**

199

200        The R-factor has been denoted by various expressions: rainfall erosivity, rainfall  
201 erosivity index, rainfall erosivity factor, rainfall erosion factor, rainfall erosion index,  
202 rainfall-runoff erosivity, rainfall erosive index, R-value, and energy-intensity. In all of these  
203 expressions, the R-factor is defined as a multiplication of the rainfall kinetic energy and  
204 rainfall intensity, based on long-term data (Wischmeier and Smith, 1958). The R-factor uses  
205 MJ mm  $ha^{-1} h^{-1} yr^{-1}$  as the SI unit; it represents the degree of soil erosivity from rainfall.

206        A number of methods for estimating the R-factor have been developed, depending on  
207 the temporal resolution of the precipitation data. These include the standard method  
208 (Wischmeier and Smith, 1978; Renard et al., 1997), simple methods (Lee and Heo, 2011),  
209 and alternative index methods (Fournier, 1960; Arnoldus, 1977). The simple and alternative  
210 index methods mainly use a rainfall parameter-based regression equation to estimate the R-  
211 factor (Meddi et al., 2016). The alternative index methods include the "KE index" method  
212 (Hudson, 1971) based on rainfall kinetic energy (E) and erodibility (K),  $AI_m$  index method  
213 (Lal, 1976) based on rainfall amount (A) and maximum rainfall intensity ( $I_m$ ), and the  
214 climatic coefficient index (Fournier, 1956). The standard method has been widely used to  
215 estimate the R-factor, as the resultant R-factor is regarded as the finest value (Lombardi Neto  
216 and Moldenhauer, 1992; Bertol et al., 2007; Meusburger et al., 2012; Panagos et al., 2016b).  
217 The standard method uses all erosive storm events, as quantified by the rainfall kinetic energy  
218 and maximum rainfall intensity over 30 min (Stocking and Elwell, 1973; Hoyos et al., 2005;  
219 Oliveira et al., 2013). The R-factors from other methods (using coarser temporal resolutions)  
220 have been compared with the results from the standard method to verify their performance.  
221 As the temporal resolution of the CMORPH is fine and sufficient for application in the  
222 standard method, this study adapts the standard method to estimate the R-factor.

223

Figure 1

224

225 Fig. 1 presents a diagram of the methodology, and consists of steps for mapping  
226 rainfall erosivity and representing the details of the classification process for an independent  
227 storm event. First, the domain fitting is trimmed to the CONUS, as the CMORPH comprises  
228 global-scale precipitation data. A threshold is applied to eliminate small amounts of rainfall  
229 arising from rainfall intermittency; this is a pre-processing step for clarifying the inter-event  
230 time definition for classification of independent rainfall pulses. The independent rainfall  
231 pulses are then classified, considering the conditions as shown in blue-line box in Fig. 1. The  
232 box illustrates the details of the classification of independent rainfall pulses. This is an  
233 important process, as it accounts for a number of effective rainfall events for estimating  
234 rainfall erosivity at each grid of the CMORPH data. Subsequently, the maximum intensity of  
235 each rainfall pulse in 30 min is extracted. The R-factor is then estimated, based on the  
236 following equation (Wischmeier and Smith, 1978; Brown and Foster, 1987; Panagos et al.,  
237 2015):

238

$$239 R = \frac{1}{n} \sum_{i=1}^n \sum_{j=1}^{m_i} (EI_{30})_j \quad (1)$$

240

241 Where,  $R$  indicates the R-factor, in  $\text{MJ mm ha}^{-1} \text{ h}^{-1} \text{ yr}^{-1}$ ;  $n$  is the number of years used to  
242 estimate the R-factor;  $m_i$  is the number of erosivity events in a given year  $i$ , and  $E$  and  $I_{30}$   
243 indicate the rainfall kinetic energy and maximum rainfall intensity in 30 min at an event  $j$ ,  
244 respectively.  $EI_{30}$  ( $\text{MJ mm ha}^{-1} \text{ h}^{-1}$ ) determines the R-factor of a single event, and is defined  
245 as follows:

246

247 
$$EI_{30} = \left( \sum_{k=1}^m e_k p_k \right) I_{30} \quad (2)$$

248

249 Where,  $e_k$  is the unit rainfall energy ( $\text{MJ ha}^{-1} \text{ mm}^{-1}$ ), and  $p_k$  is the  $k$ -th rainfall volume (mm)  
 250 of a storm event including  $m$  parts.  $k$  is the time period of each rainfall, and  $m$  is the duration  
 251 of the storm event.

252 The unit rainfall energy is estimated using a rainfall intensity-energy equation derived  
 253 from Van Dijk et al. (2002). The equation was verified in a number of previous studies  
 254 (Marques et al., 2007; Vrieling et al., 2010). The rainfall intensity-energy equation used in  
 255 this study is as follows:

256

257 
$$e_k = 28.3[1 - 0.52\exp(-0.042I)] \quad (3)$$

258

259 Where,  $I$  is the rainfall intensity ( $\text{mm hr}^{-1}$ ). As the R-factor is estimated based on each grid,  
 260 the final R-factor map is visualized with colors representing corresponding values.

261

262 **3. Results**

263

264 **3.1 Annual and Monthly Rainfall Erosivity Maps over the CONUS**

265

266 The annual R-factors from 1998–2015 were estimated using the CMORPH  
 267 precipitation product and standard method. Fig. 2 shows the number of identified storm  
 268 events, annual precipitation, and R-factors for each year. Overall, the results demonstrate that  
 269 the trends of the annual precipitation and number of storms are similar to the increasing and  
 270 decreasing patterns of the annual R-factor. In 1998, 2004, 2009, and 2015, i.e., where the R-

271 factor was higher than other years, the number of storm events and annual precipitation were  
272 also higher than in the other years. The mean annual number of storms ranges from 25 to 30,  
273 the mean value of annual precipitation ranges from 570 to 770 mm, and the mean annual R-  
274 factor ranges from 920 to 1420 MJ mm  $ha^{-1} h^{-1} yr^{-1}$ .

275

Figure 2

276

277 Fig. 3 shows the rainfall erosivity map for the United States, and a probability density  
278 function of the R-factors. The rainfall erosivity map was presented at an 8 km  $\times$  8 km spatial  
279 resolution. The mean of the rainfall erosivity is 1,260 MJ mm  $ha^{-1} h^{-1} yr^{-1}$  with high  
280 variability, as expressed by the standard deviation of 1,037 MJ mm  $ha^{-1} h^{-1} yr^{-1}$ . The median  
281 (50th percentile) of the R-factor is 1,100 MJ mm  $ha^{-1} h^{-1} yr^{-1}$ . The bottom 20% of the R-  
282 factors are lower than 357 MJ mm  $ha^{-1} h^{-1} yr^{-1}$ , and the highest 20% (80th percentile) are  
283 greater than 2,200 MJ mm  $ha^{-1} h^{-1} yr^{-1}$  (see Fig. 3b).

284

Figure 3

285

286 The range of the R-factor is from 33 to 6,000 MJ mm  $ha^{-1} h^{-1} yr^{-1}$ , and it varies  
287 considerably with region. As expected, the results indicate that the high values of the R-factor  
288 are estimated mainly around the coastal regions. The highest 20% (of the R-factor) is  
289 estimated from the coastal regions of the Pacific Ocean, Gulf of Mexico, Florida Peninsula,  
290 and Atlantic Ocean. Among the coastal regions, for example, the western north region (in  
291 contact with the North Pacific Ocean) is vulnerable to soil erosion by rainfall, as this region  
292 has seasonal and extreme rainfall storms (e.g., atmospheric rivers) routinely inflowing into

293 the regions during winter. Moreover, high rainfall intensity is commonly observed, owing to  
294 complex terrain (Han et al., 2019). Along the same lines, the spatial patterns of rainfall  
295 erosivity in a chain of mountains in the western/north United States were completely different  
296 between the western (complex terrain) and eastern (flat terrain) regions.

297 The map demonstrates that the inland and coastal regions affected by the various  
298 types of storms from the Gulf of Mexico and Atlantic Ocean have high R-factor values. The  
299 coastal regions of the Gulf of Mexico and Atlantic Ocean have a long history of hurricanes  
300 and tropical storms, as the climatologically warm seawater provides an abundant energy  
301 source for intense storms during the hurricane season from May to November (Jarvinen et al.,  
302 1984; Maloney and Hartmann, 2000). Thus, hurricanes and tropical storms could easily move  
303 into the inland areas and deliver heavy rainfalls, owing to the warm sea temperature and flat  
304 terrain (Bales, 2003; Stanturf et al., 2007). Except for the regions mentioned above, the  
305 spatial patterns of the R-factor are homogeneous over the United States, and the R-factors are  
306 not excessively high compared to the coastal regions.

307

Figure 4

308

309 Fig. 4 shows the monthly rainfall erosivity maps. The intensity of the monthly R-  
310 factor apparently varies with the regional seasonality. For example, the west coastal region  
311 showed high rainfall erosivity during a winter season from November to March, and the R-  
312 factor was identified in December. However, during the summer and early fall seasons from  
313 June to September, the rainfall erosivity was low and spatially homogeneous. In addition, the  
314 monthly rainfall erosivity maps exhibited a smooth decrease in the R-factor from winter to  
315 spring, followed by lower homogeneous values in summer, and then a smooth increase in fall.  
316 As expected, the results suggest that the trend of rainfall erosivity is affected by the

317 seasonality, as is the case with precipitation. In the coastal and inland regions near the Gulf of  
318 Mexico, the spatial distribution of the R-factor was inhomogeneous, and the value was very  
319 high from June to December. The period from June to September showed conflicting  
320 tendencies in rainfall erosivity between the western and eastern coastal regions. In addition,  
321 the R-factors in the Florida Peninsula were significantly higher from June to September.

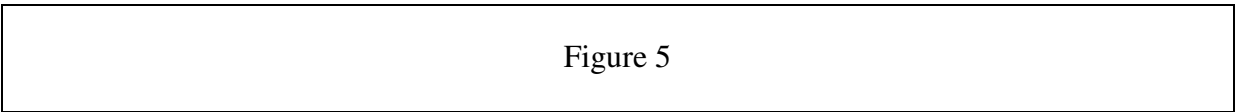
322

### 323 **3.2 Attributes of Rainfall Erosivity on Hydrological Basins and Climate Zones**

324

325 The rainfall erosivity map was further analyzed in the context of hydrological unit  
326 basins and climatological zones. For this purpose, the hydrologic unit code-2 (HUC,  
327 <https://water.usgs.gov//GIS/huc.html>) and climate features (hereinafter referred to as climate  
328 zones) developed by Wladimir Köppen (Kottek et al., 2006) were used. This section  
329 addresses the analysis results for the hydrological unit basins. Fig. 5 shows the HUC  
330 boundary (the upper left), its area distribution (the upper right), and R-factors (the bottom).  
331 The HUC includes the Tennessee region, i.e., the smallest basin (105,949 sq. km), and the  
332 Missouri region, i.e., the biggest basin (1,349,418 sq. km, or 15% of the total area).

333

334 Figure 5

335

336 The range of the R-factors varies with the location of the basin. The ‘a’-‘h’ (except ‘d’  
337 and ‘g’) basins, located on the Florida Peninsula and influenced by the climates of the  
338 Atlantic Ocean and Gulf of Mexico, have high rainfall erosivity. ‘h’ (lower Mississippi  
339 region) represents the basin where the highest R-factor was identified. However, the ‘n’  
340 (upper Colorado region), ‘o’ (lower Colorado region), and ‘p’ (great basin region) basins had  
relatively low values of the R-factor. Considering the ranges of the R-factors in the three

341 basins, the spatial distributions of the R-factors in these basins were considerably  
342 homogenous. 'j' (Missouri region), the largest basin in the United States, had a relatively  
343 narrow range for the R-factor, indicating a low variation and spatially homogeneous  
344 distribution. Both 'k' (Arkansas-White-Red region) and 'i' (Texas-Gulf region) were smaller  
345 than 'j'; both basins had a wider range of the R-factors than 'j', and spatially inhomogeneous  
346 distributions.

347

Figure 6

348

349 Fig. 6 illustrates the results for monthly R-factors by basin, to show the seasonal  
350 patterns of the R-factors. Most basins showed a change of rainfall erosivity with season. In  
351 particular, some basins ('a'- 'i') located on the east coast line had a high rainfall erosivity  
352 from June to September, whereas it was low in January, February, and December. Basins ('q'  
353 and 'r') located on the west coastline showed a high rainfall erosivity during the winter  
354 season (from November to March), but showed a low rainfall erosivity during the warm  
355 season (from April to September). 'h' had high R-factor values for all months. Compared  
356 with other basins, 'c' (South Atlantic-Gulf region) had the highest values of the R-factor from  
357 June to September. The monthly R-factors of 'n', 'o', and 'p' were consistent, as the range  
358 was only from 3 to 52, and it was not varied from month-to-month. These results suggest that  
359 those basins show no seasonality in rainfall erosivity.

360 The rainfall erosivity map is also analyzed based on climate zones. Fig. 7 shows a  
361 map of climate zones in the United States, and the distribution of the R-factor by the climate  
362 zones. Over the CONUS, five (Cfa, BSk, Dfb, Dfa, and Csb) of climate zones are complexly  
363 distributed in the western region, whereas three (Cfa, Dfa, and Dfb) climate zones are  
364 homogeneously distributed in the eastern region (depending on the latitude).

365

Figure 7

366

367        The tropical climate zones have the highest R-factor, followed by the temperate, cold,  
368        and arid climate groups. On average, 45 annual mean storm events with sufficient intensity to  
369        erode soil were observed in the tropical climate group (covering most of the southern Florida  
370        Peninsula). This was 1.5 times higher than the number of annual mean storm events in the  
371        United States. The temperate climate zones (covering most of the regions affected by storms  
372        from the Gulf of Mexico and Atlantic Ocean) had relatively high rainfall erosivity. Moreover,  
373        15 of the annual mean storm events were observed in the arid climate group, which showed  
374        the lowest rainfall erosivity within 15 of the climate zones. That was only approximately half  
375        the number of annual mean storm events in the United States.

376

Figure 8

377

378        Fig. 8 shows the monthly rainfall erosivity by climate zone. The seasonality of the R-  
379        factor was clearly visible in the tropical climate group. The high values of the R-factor (mean  
380        =  $492 \text{ MJ mm ha}^{-1} \text{ hr}^{-1} \text{ month}^{-1}$ ) were identified during the wet season from June to  
381        September, whereas the low values of the R-factor (mean =  $108 \text{ MJ mm ha}^{-1} \text{ hr}^{-1} \text{ month}^{-1}$ )  
382        were found during a dry season from November to April. However, the arid climate zone  
383        showed no seasonality in regards to the rainfall erosivity.

384

### 385        **3.3 Comparison with the Ground-Based Rainfall Erosivity Map**

386

387 To evaluate the rainfall erosivity map developed in this study, it was compared to a  
388 rainfall erosivity map based on rain-gauge data (Fig. 9). Panagos et al. (2017) developed a  
389 global rainfall erosivity map using high-resolution rain-gauge data collected from 65  
390 countries as a reference. For the United States, they employed 92 pieces of gauge data over  
391 11 years (2006–2016). The average density of the observation stations was one every 83,303  
392 km<sup>2</sup>. They used a Gaussian process regression model to interpolate the R-factor point values  
393 to a map at a 1 km × 1 km spatial resolution. This map is available from the European Soil  
394 Data Centre (<https://esdac.jrc.ec.europa.eu/content/global-rainfall-erosivity>).  
395

396  
397 Figure 9

398 The range of the R-factors in Panagos et al. (2017) is 6–9,645 MJ mm ha<sup>-1</sup> h<sup>-1</sup> yr<sup>-1</sup>,  
399 and the mean value is 2,067 MJ mm ha<sup>-1</sup> h<sup>-1</sup> yr<sup>-1</sup>, i.e., 1.65 times higher than the mean R-  
400 factor estimated in this study. In Fig. 9, the western north region (a), middle region (b), and  
401 coastal and inland region near by Gulf of Mexico (c) were highlighted for comparison. The  
402 R-factors in box (a), as estimated in this study, are higher than those from Panagos et al.  
403 (2017). Considering the comparison result of the annual precipitations in Fig. 8, this result  
404 demonstrates that the R-factors calculated by Panagos et al. (2017) were far more  
405 underestimated than those in this study. This is because Panagos et al. (2017) only used three  
406 rain-gauge sites to cover the region. Notably, the spatial distribution of the rainfall erosivity  
407 estimated in this study is more seamless than that in Panagos et al. (2017), even though the  
408 spatial resolution of this study (8 × 8 km) is coarser than that of Panagos et al. (2017) (1 × 1  
409 km), especially for the box (c) regions close to the Gulf of Mexico. This result exhibits the  
410 typical limitations in using rain-gauge data and interpolation methods for predicting R-factors  
in ungauged areas.

411 The bottom-left panel in Fig. 9 shows a comparison of R-factor samplings extracted  
412 from 10,000 random points. The R-squared value is 0.64, and the bias is 64%. Based on the  
413 Y-axis (the R-factors of Panagos et al. (2017)), the bias is 88.1% when the R-factor is smaller  
414 than 2,000, whereas the bias is 55.6% when the R-factor is greater than 2,000. This result  
415 suggests that the larger the estimated R-factors, the higher the uncertainty. Considering that  
416 the R-factors greater than 2,000 are mostly from the coastal regions, data assimilation with  
417 high-density rain-gauge data might be necessary in these regions to improve the accuracy of  
418 the predicted R-factor.

419

#### 420 **4. Discussion**

##### 421 **4.1 The CMORPH for Mapping Rainfall Erosivity**

422

423 With regard to hydrologic applications, many studies have evaluated the CMORPH product  
424 against ground-based observations and "Next Generation Weather Radar" Stage IV (radar-  
425 based and gauge-adjusted) as reference data (Derin et al., 2016). According to AghaKouchak  
426 et al. (2011) and Romilly and Gebremichael (2011), the CMORPH data is superior to that  
427 from other satellite precipitation products (e.g., "PERSIANN," "TMPA-RT," and TMPA-V6)  
428 with respect to the probability of detecting extremes and the volume of correctly identified  
429 precipitation. When applying CMORPH in Ethiopian river basins, the volume of precipitation  
430 tends to be underestimated by 11%, and the bias depends on the rainfall regime and  
431 topographical characteristics. Habib et al. (2012) evaluated the CMORPH using dense ground  
432 observations in south Louisiana, and suggested that the CMORPH product has high detection  
433 skills. In particular, they suggested that the probability of successful detection is approximately 80% for surface rain rates  $>2$  mm/h, the probability of false detection is <3%,

435 and the CMORPH has a negligible bias. However, they also concluded that the accuracy of  
436 the CMORPH products varied with temporal resolution, region, and season.

437

Figure 10

438

439 As the CMORPH is a satellite-based precipitation product, it might incorporate  
440 several uncertainties that might influence the estimation and mapping of the R-factors. In this  
441 study, we intend to highlight two issues: overestimated precipitation on water bodies (e.g.,  
442 lakes and reservoirs), and the accuracy of annual precipitation. It is well-known that satellite-  
443 based precipitation products are likely to overestimate precipitation where lakes and  
444 reservoirs are located (Tian and Peters-Lidard, 2007). This fact is also confirmed in this study.  
445 Fig. 10 shows (a) a map showing the locations of water bodies on the annual precipitation  
446 field, and (b) the rainfall erosivity map. It is found that the annual precipitation on water  
447 bodies is abnormally higher than in other areas. It is also confirmed that the R-factor result  
448 shows the same trend for water bodies. In view of this attribute of the CMORPH precipitation  
449 product, this study excluded the abnormally overestimated R-factors for water bodies from  
450 further analysis.

451 To briefly verify the accuracy of the CMORPH precipitation, this study compared the  
452 CMORPH and "PRISM" (<http://www.prism.oregonstate.edu/>), a rain gauge-based  
453 precipitation product. Fig. 11 shows three comparison results: spatial distributions (top left  
454 panel), probability density functions (top right panel), and samples extracted from 10,000  
455 random points (bottom panel).

456

Figure 11

457

458 In the spatial distribution maps, three regions are selected, i.e., boxes (a), (b), and (c).

459 Overall, the trends of the spatial distributions are similar to each other, and the correlation of  
460 the two maps reaches as high as 0.71. In the case of box (b), in the middle of the country, and  
461 box (c), affected by Atlantic Ocean and Gulf of Mexico, both annual precipitation maps show  
462 similar patterns of spatial distributions and PDFs (top panels). However, box (a), close to the  
463 Pacific Ocean, shows that the CMORPH was underestimated as compared to that of PRISM,  
464 and the difference was up to approximately double. Considering this result, the rainfall  
465 erosivity map based on the CMORPH has a higher possibility of underestimation around the  
466 region. Data assimilation with rain-gauge data might be a way to overcome this limitation of  
467 the CMORPH, and to improve the quantitative accuracy of the precipitation product for  
468 mapping rainfall erosivity. As this topic is challenging and out of scope for this study, we  
469 leave this issue for future study.

470 According to the result in Fig. 11 (bottom panel), the R-squared value is as high as  
471 0.67 and the bias is 84%, indicating an ideal case. It is confirmed that the scatter samples  
472 where the PRISM is greater than the CMORPH are mostly extracted from box (a). Thus, the  
473 accuracy of satellite-based precipitation data can be lower than that of the rain-gauge data,  
474 but can help overcome the aforementioned limitations in the rain-gauge data. Considering the  
475 pace of technological developments in satellite observation systems and data quality  
476 improvements, satellite-based precipitation data should be the best alternative to a ground-  
477 based observation system in the future.

478

479 **4.2 Potential Benefit of the Rainfall Erosivity Map in Practice**

480

481 Considering the effects of soil erosion by rainfall on the entire environment, it is  
482 expected that the rainfall erosivity map developed in this study can be used to estimate  
483 amounts of soil loss, and to identify regions vulnerable to soil erosion. The 1972 amendments  
484 to the Clean Water Act (CWA) prohibit the discharge of any pollutant into navigable waters,  
485 unless the discharge is authorized by a National Pollutant Discharge Elimination System  
486 (NPDES) permit. As construction site stormwater runoff can contribute significantly to water  
487 quality problems, the Phase I Stormwater Rule required that all construction sites with a  
488 planned land disturbance of five acres or more must obtain an NPDES permit and implement  
489 stormwater runoff control plans. Phase II extended the requirements of the stormwater  
490 program to sites between 1–5 acres (EPA, 2012). The rainfall erosivity waiver allows the  
491 permitting authorities to waive the requirements for those sites that do not have adverse water  
492 quality impacts. The United States Environmental Protection Agency (EPA) NPDES has  
493 developed a web-based R-factor estimation tool for users attempting to implement the CWA  
494 (<https://www.epa.gov/waterdata/rainfall-erosivity-factor-calculator>). However, it is  
495 questionable whether the tool can estimate a proper R-factor in a certain area, as the tool is  
496 based on rain-gauge data and a spatial interpolation method. Therefore, at this point, the  
497 rainfall erosivity map developed in this study could practically improve or replace the EPA  
498 NPDES R-factor map.

499

500

## 501 **5. Conclusions**

502

503 This study suggested a new approach for mapping rainfall erosivity using a high-  
504 resolution satellite-based precipitation product, and applied it to the CONUS. The rainfall  
505 erosivity map was analyzed in terms of different temporal resolutions (e.g., monthly and

506 annual rainfall erosivity), hydrological unit basins, and climate zones. Based on the results,  
507 we concluded as follows:

- 508 · Using the CMORPH (a high-resolution satellite-based data) to map rainfall  
509 erosivity has strengths and weaknesses. The CMORPH was able to apply the  
510 standard method to estimate a relatively accurate R-factor, and to map a  
511 seamless rainfall erosivity without employing an interpolation method. These  
512 merits were useful for understanding the spatial variability of rainfall erosivity,  
513 and for identifying regions vulnerable to soil erosion by rainfall. However, the  
514 CMORPH precipitation product might require correction for some coastal  
515 regions to improve the rainfall erosivity map.
- 516 · From the rainfall erosivity map, the mean of the rainfall erosivity was 1,260  
517 MJ mm  $ha^{-1} h^{-1} yr^{-1}$ , with high variability ranging from 33 to 6,000 MJ mm  $ha^{-1}$   
518  $h^{-1} yr^{-1}$ , depending on the region of the United States. The coastal regions  
519 near the Pacific Ocean, Gulf of Mexico, and Atlantic Ocean have the highest  
520 20% of rainfall erosivity. The seasonality of rainfall erosivity was confirmed  
521 through the monthly rainfall erosivity maps. Most coastal regions are  
522 vulnerable to soil erosion by rainfall, depending on their typical rainy seasons.  
523 In addition, climate features have a strong relation with rainfall erosivity, and  
524 the spatial pattern of rainfall erosivity varies within climate zones. The rainfall  
525 erosivity in the tropical climate group was relatively higher than that in the  
526 other groups, whereas the arid climate group presented very low and spatially  
527 homogeneous rainfall erosivity. Soil loss should be monitored in coastal  
528 regions, and construction areas should be thoroughly examined in the southern  
529 Florida Peninsula belonging to the tropical climate group.

530

531        Finally, considering the pace of technological developments in satellite observation  
532    systems and data quality improvements, satellite-based rainfall erosivity maps represent the  
533    best alternative to ground-based rainfall erosivity maps in the future.

534

535    Acknowledgements

536    This work was supported by the NOAA Physical Sciences Division. Jungho Kim  
537    acknowledges support from NOAA Hydro-meteorological research program. We appreciate  
538    the internal reviewer contribution from Lynn Johnson.

539

540    **References**

541

542    AghaKouchak, A., Behrangi, A., Sorooshian, S., Hsu, K., Amitai, E., 2011. Evaluation of  
543        satellite-retrieved extreme precipitation rates across the central United States. *J.*  
544        *Geophys. Res.* 116, D02115. <https://doi.org/10.1029/2010JD014741>.

545    Ahn, K. H., Palmer, R. N., 2015. Trend and variability in observed hydrological extremes in  
546        the United States. *J. Hydrol. Eng.* 21(2), 04015061.  
547        [https://doi.org/10.1061/\(ASCE\)HE.1943-5584.0001286](https://doi.org/10.1061/(ASCE)HE.1943-5584.0001286).

548    Anagnostou, E. N., Maggioni, V., Nikolopoulos, E. I., Meskele, T., Hossain, F.,  
549        Papadopoulos, A., 2010. Benchmarking high-resolution global satellite rainfall  
550        products to radar and rain-gauge rainfall estimates. *IEEE T. Geosci. Remote.* 48(4),  
551        1667-1683. [10.1109/TGRS.2009.2034736](https://doi.org/10.1109/TGRS.2009.2034736).

552    Angulo-Martínez, M., Beguería, S., 2009. Estimating rainfall erosivity from daily  
553        precipitation records: A comparison among methods using data from the Ebro Basin  
554        (NE Spain). *J. Hydrol.* 379(1-2), 111-121.  
555        <https://doi.org/10.1016/j.jhydrol.2009.09.051>.

556 Arnoldus, H.M.J., 1977. Methodology used to determine the maximum potential average  
557 annual soil loss due to sheet and rill erosion in Morocco. FAO Soils Bull. 34, 83.

558 Bales, J. D., 2003. Effects of hurricane floyd inland flooding, September–October 1999, on  
559 tributaries to Pamlico Sound, North Carolina. Estuaries, 26(5), 1319-1328.

560 Ballabio, C., Borrelli, P., Spinoni, J., Meusburger, K., Michaelides, S., Beguería, S., Klik, A.,  
561 Petan, S., Janeček, M., Olsen, P., Aalto, J., 2017. Mapping monthly rainfall erosivity in  
562 Europe. Sci. Total. Environ. 579, 1298-1315.  
563 <https://doi.org/10.1016/j.scitotenv.2016.11.123>.

564 Bertol, I., Leite, D., Engel, F.L., Cogo, N.P., González, A.P., 2007. Erodibility of a  
565 typichapludox evaluated underfield conditions. Revista Brasileira de Ciência do Solo31,  
566 541–549. <http://dx.doi.org/10.1590/S0100-06832007000300014>.

567 Bonilla, C. A., Vidal, K. L., 2011. Rainfall erosivity in central Chile. J. Hydrol. 410(1-2),  
568 126-133. <https://doi.org/10.1016/j.jhydrol.2011.09.022>.

569 Brown, L. C., Foster, G. R., 1987. Storm erosivity using idealized intensity distributions. T.  
570 ASAE. 30(2), 379-0386. <https://doi.org/10.13031/2013.31957>.

571 Buytaert, W., Celleri, R., Willems, P., De Bievre, B., Wyseure, G., 2006. Spatial and  
572 temporal rainfall variability in mountainous areas: A case study from the south  
573 Ecuadorian Andes. J. Hydrol. 329(3-4), 413-421.  
574 <https://doi.org/10.1016/j.jhydrol.2006.02.031>.

575 Chen, H., Chandrasekar, V., Cifelli, R., Xie, P., 2019. A Machine Learning System for  
576 Precipitation Estimation Using Satellite and Ground Radar Network Observations,  
577 IEEE Trans. Geosci. Remote Sens. <https://doi.org/10.1109/TGRS.2019.2942280>.

578 Conner, W. H., Day, J. W., Baumann, R. H., Randall, J. M., 1989. Influence of hurricanes on  
579 coastal ecosystems along the northern Gulf of Mexico. Wetl. Ecol. Manag. 1, 45–56.  
580 <https://doi.org/10.1007/BF00177889>.

581 Cooper, K., 2011. Evaluation of the relationship between the RUSLE R-factor and mean  
582 annual precipitation. Research Report, Colorado State University:  
583 [https://www.enr.colostate.edu/~pierre/ce\\_old/Projects/linkfiles/Cooper%20R-factor-Final.pdf](https://www.enr.colostate.edu/~pierre/ce_old/Projects/linkfiles/Cooper%20R-factor-Final.pdf).

585 Da Silva, A. M., 2004. Rainfall erosivity map for Brazil. *Catena* 57(3), 251-259.  
586 <https://doi.org/10.1016/j.catena.2003.11.006>.

587 Derin, Y., Anagnostou, E., Berne, A., Borga, M., Boudevillain, B., Buytaert, W., Chang, C.H.,  
588 Delrieu, G., Hong, Y., Hsu, Y.C. and Lavado-Casimiro, W., Mane, B., Moges, S.,  
589 Nikolopoulos, E. I., Sahlu, D., Salerno, F., Juan-Pablo Rodríguez-Sánchez, Vergara, H.  
590 J., Yilmaz, K. K., 2016. Multiregional satellite precipitation products evaluations over  
591 complex terrain. *J. Hydrometeorol.* 17, 1817-1836. <https://doi.org/10.1175/JHM-D-15-0197.1>.

593 Elbasit, A. M. A., Huang, J., Ojha, C. S. P., Yasuda, H., Adam, E. O., 2013. Spatiotemporal  
594 changes of rainfall erosivity in Loess Plateau. *China. ISRN Soil Science.* 2013.  
595 <http://dx.doi.org/10.1155/2013/256352>.

596 Elwell, H. A., Stocking, M. A., 1976. Vegetal cover to estimate soil erosion hazard in  
597 Rhodesia. *Geoderma.* 15(1), 61-70. [https://doi.org/10.1016/0016-7061\(76\)90071-9](https://doi.org/10.1016/0016-7061(76)90071-9).

598 Fournier, F., 1956. The effect of climatic factors on soil erosion. Estimates of solids  
599 transported in suspension in runoff. *Ass. Int. Hydrol. Publ.* 38, 6.

600 Fournier, F., 1960. *Climat et Erosion*, Presses Universitaires de France, Paris.

601 Goovaerts, P., 1999. Using elevation to aid the geostatistical mapping of rainfall erosivity.  
602 *Catena* 34(3-4), 227-242. [https://doi.org/10.1016/S0341-8162\(98\)00116-7](https://doi.org/10.1016/S0341-8162(98)00116-7).

603 Habib, E., Haile, A. T, Tian, Y., Joyce, R. J., 2012. Evaluation of the high-resolution  
604 CMORPH satellite rainfall product using dense rain gauge observations and radar-  
605 based estimates. *J. Hydrometeorol.* 13, 1784-1798. <https://doi.org/10.1175/JHM-D-12->

606 017.1.

607 Han, H., Kim, J., Chandrasekar, V., Choi, J., Lim, S., 2019. Modeling streamflow enhanced  
608 by precipitation from atmospheric river using the NOAA national water model: a case  
609 study of the Russian river basin for February 2004. *Atmos.* 10 (8), 466.  
610 <https://doi.org/10.3390/atmos10080466>.

611 Hernando, D., Romana, M. G., 2015. Estimating the rainfall erosivity factor from monthly  
612 precipitation data in the Madrid Region (Spain). *J. Hydrol. Hydromech.*, 63 (1), 55-62.  
613 <https://doi.org/10.1515/johh-2015-0003>.

614 Hoyos, N., Waylen, P.R., Jaramillo, A., 2005. Seasonal and spatial patterns of erosivity in a  
615 tropical watershed of the Colombian Andes. *J. Hydrol.* 314, 177–191.  
616 <http://dx.doi.org/10.1016/j.jhydrol.2005.03.014>.

617 Hudson, N., 1971. *Soil Conservation*. Cornell University Press, Ithaca.

618 Jarvinen, B. R., Neumann, C. J., Davis, M. A., 1984. A tropical cyclone data tape for the  
619 North Atlantic Basin, 1886-1983: Contents, limitations, and uses.

620 Jayawardena, A. W., Rezaur, R. B., 2000. Drop size distribution and kinetic energy load of  
621 rainstorms in Hong Kong. *Hydrol. Process.* 14(6), 1069-1082.  
622 [https://doi.org/10.1002/\(SICI\)1099-1085\(20000430\)14:6<1069::AID-HYP997>3.0.CO;2-Q](https://doi.org/10.1002/(SICI)1099-1085(20000430)14:6<1069::AID-HYP997>3.0.CO;2-Q).

624 Joyce, R. J., Janowiak, J. E., Arkin, P. A., Xie, P., 2004. CMORPH: A method that produces  
625 global precipitation estimates from passive microwave and infrared data at high spatial  
626 and temporal resolution. *J. Hydrometeorol.* 5(3), 487-503.  
627 [https://doi.org/10.1175/1525-7541\(2004\)005<0487:CAMTPG>2.0.CO;2](https://doi.org/10.1175/1525-7541(2004)005<0487:CAMTPG>2.0.CO;2).

628 Khorsandi, N., Mahdian, M. H., Pazira, E., Nikkami, D., Chamheidar, H., 2012. Comparison  
629 of Different Interpolation Methods for Investigating Spatial Variability of Rainfall  
630 Erosivity Index. *Pol. J. Environ. Stud.* 21(6).

631 Kim, J., Yoo, C., 2014. Use of a dual Kalman filter for real-time correction of mean field bias  
632 of radar rain rate. J. Hydrol. 519(Part D), 2785-2796.  
633 <http://doi.org/10.1016/j.jhydrol.2014.09.072>.

634 Kim, J., Yoo, C., Lim, S., Choi, J., 2015. Usefulness of relay-information-transfer for radar  
635 QPE. J. Hydrol. 531, 308-319. <https://doi.org/10.1016/j.jhydrol.2015.07.006>.

636 Klik, A., Haas, K., Dvorackova, A., Fuller, I. C., 2015. Spatial and temporal distribution of  
637 rainfall erosivity in New Zealand. Soil. Res. 53(7), 815-825.  
638 <https://doi.org/10.1071/SR14363>.

639 Knight, D. B., Davis, R. E., 2007. Climatology of tropical cyclone rainfall in the southeastern  
640 United States. Phys. Geogr., 28(2), 126-147. <https://doi.org/10.2747/0272-3646.28.2.126>

642 Kotttek, M., Grieser, J., Beck, C., Rudolf, B., Rubel F., 2006. World Map of the Köppen-  
643 Geiger climate classification updated. Meteorol. Z. 15, 259-263.  
644 <https://doi.org/10.1127/0941-2948/2006/0130>.

645 Krauer, J., 1988. Rainfall, erosivity and isoerodent map of Ethiopia.

646 Lal, R., 1976. Soil erosion on alfisols in Western Nigeria III—Effects of rainfall character-  
647 istics. Geoderma 16, 389–401. [http://dx.doi.org/10.1016/0016-7061\(76\)90003-3](http://dx.doi.org/10.1016/0016-7061(76)90003-3).

648 Lal, R., 2005. Soil erosion and carbon dynamics, Soil. Till. Res. 81(2), 137-142.  
649 <https://doi.org/10.1016/j.still.2004.09.002>.

650 Lee, J., Heo, J., 2011. Evaluation of estimation methods for rainfall erosivity based on annual  
651 precipitation in Korea, J. Hydrol. 409, 30-48.  
652 <https://doi.org/10.1016/j.jhydrol.2011.07.031>.

653 Lee, M. H., Lin, H. H., 2015. Evaluation of annual rainfall erosivity index based on daily,  
654 monthly, and annual precipitation data of rainfall station network in Southern Taiwan.  
655 International Journal of Distributed Sensor Networks, 11(6), 214708.

656 <https://doi.org/10.1155/2015/214708>.

657 Lenvain, J. S., Sakala, W. K., Pauwelyn, P. L. L., 1988. Iso-erodent map of Zambia: Part II:

658 Erosivity prediction and mapping. *Soil. Technol.* 1(3), 251-262.

659 [https://doi.org/10.1016/0933-3630\(88\)90024-4](https://doi.org/10.1016/0933-3630(88)90024-4).

660 Leow, C. S., Ghani, A. A., Zakaria, N. A., Abidin, R. Z., 2011. Development of rainfall

661 erosivity isohyet map for Peninsular Malaysia. In 3rd International Conference on

662 Managing Rivers in the 21st Century: Sustainable Solutions for Global Crisis of

663 Flooding, Pollution and Water Scarcity, 748-756.

664 Lombardi Neto, F., Moldenhauer, W.C., 1992. Rainfall erosivity—its distribution

665 and relationship with soil loss at Campinas, state of São Paulo, Brazil. *Bragantia*, 51,

666 189–196. <http://dx.doi.org/10.1590/S0006-87051992000200008>.

667 LOWLAND, P. O. S. S., 2005. Artificial neural networks use for rainfall-runoff erosivity

668 factor estimation. *Environ. Dev.* 8(1), 04.

669 Maloney, E. D., Hartmann, D. L., 2000. Modulation of eastern North Pacific hurricanes by

670 the Madden–Julian oscillation. *J. climate*, 13(9), 1451-1460.

671 Marques, M.J., Bienes, R., Jimenez, L., Perez-Rodriguez, R., 2007. Effect of vegetal cover

672 on runoff and soil erosion under light intensity events. *Rainfall simulation over*

673 *USLEplots. Sci. Total Environ.* 378 (1–2), 161–165.

674 <https://doi.org/10.1016/j.scitotenv.2007.01.043>.

675 Meddi, M., Toumi, S., Assani, A. A., 2016. Spatial and temporal variability of the rainfall

676 erosivity factor in Northern Algeria. *Arab. J. Geosci.* 9(4), 282.

677 <https://doi.org/10.1007/s12517-015-2303-8>.

678 Meusburger, K., Steel, A., Panagos, P., Montanarella, L., Alewell, C., 2012. Spatial and

679 temporal variability of rainfall erosivity factor for Switzerland. *Hydro. Earth. Syst. SC.*

680 16(1), 167-177. doi:10.5194/hess-16-167-2012.

681 Mikhailova, E. A., Bryant, R. B., Schwager, S. J., Smith, S. D., 1997. Predicting rainfall  
682 erosivity in Honduras. *Soil. Sci. Soc. Am. J.* 61(1), 273-279.  
683 <https://doi.org/10.2136/sssaj1997.03615995006100010039x>.

684 Nearing, M. A., Lane, L. J., Lopes, V. L., 1994. Modeling soil erosion. *Soil erosion research*  
685 methods. 2, 127-156.

686 Nesbitt, S. W., Anders, A. M., 2009. Very high resolution precipitation climatologies from  
687 the Tropical Rainfall Measuring Mission precipitation radar. *Geophys. Res. Lett.*  
688 36(15). <https://doi.org/10.1029/2009GL038026>.

689 Niedermeier, C., 1998. Soil erosion modeling using GIS.

690 Odudo-Afriyie, K., 1996. Rainfall erosivity map for Ghana. *Geoderma*. 74(1-2), 161-166.  
691 [https://doi.org/10.1016/S0016-7061\(96\)00054-7](https://doi.org/10.1016/S0016-7061(96)00054-7).

692 Odudo-Afriyie, K., 1998. Rainfall erosivity map for West Africa. *J. Appl. Sci. Tech.* 3(1-2),  
693 92-101.

694 Oliveira, P. T. S., Wendland, E., Nearing, M. A., 2013. Rainfall erosivity in Brazil: A  
695 review. *Catena*, 100, 139-147. <https://doi.org/10.1016/j.catena.2012.08.006>.

696 Panagos, P., Ballabio, C., Borrelli, P., Meusburger, K., Klik, A., Rousseva, S., Tadić, M.P.,  
697 Michaelides, S., Hrabalíková, M., Olsen, P., Aalto, J., Lakatos, M., Rymaszewicz, A.,  
698 Dumitrescu, A., Beguería, S., Alewell, C., 2015. Rainfall erosivity in Europe. *Sci. Total Environ.* 511, 801-814. <https://doi.org/10.1016/j.scitotenv.2015.01.008>.

700 Panagos, P., Ballabio, C., Borrelli, P., Meusburger, K., 2016a. Spatio-temporal analysis of  
701 rainfall erosivity and erosivity density in Greece. *Catena* 137, 161-172.  
702 <https://doi.org/10.1016/j.catena.2015.09.015>.

703 Panagos, P., Borrelli, P., Spinoni, J., Ballabio, C., Meusburger, K., Beguería, S., Klik, A.,  
704 Michaelides, S., Petan, S., Hrabalíková, M., Olsen, P., Aalto, J., Lakatos, M.,  
705 Rymaszewicz, A., Dumitrescu, A., Tadić, M. P., Diodato, N., Kostalova, J., Rousseva,

706 S., Banasik, K., Alewell, C., 2016b. Monthly rainfall erosivity: conversion factors for  
707 different time resolutions and regional assessments. *Water.* 8(4), 119.  
708 <https://doi.org/10.3390/w8040119>.

709 Panagos, P., Borrelli, P., Meusburger, K., Yu, B., Klik, A., Lim, K.J., Yang, J.E., Ni, J., Miao,  
710 C., Chattopadhyay, N., Sadeghi, S.H., Hazbavi, Z., Zabihi, M., Larionov, G. A.,  
711 Krasnov, S. F., Gorobets, A. V., Levi, Y., Erpul, G., Birkel, C., Hoyos, N., Naipal, V.,  
712 Oliveira, P. T. S., Bonilla, C. A., Meddi, M., Nel, W., Dashti, H. A., Boni, M., Diodato,  
713 N., Oost, K. V., Nearing, M., Ballabio, C., 2017. Global rainfall erosivity assessment  
714 based on high-temporal resolution rainfall records. *Sci Rep.* DOI:10.1038/s41598-017-  
715 04282-8.

716 Ralph, F.M., Neiman, P.J., Wick, G.A., Gutman, S.I., Dettinger, M.D., Cayan, D.R., White,  
717 A.B., 2006. Flooding on California's Russian River: Role of atmospheric rivers.  
718 *Geophys. Res. Lett.*, 33. <https://doi.org/10.1029/2006GL026689>.

719 Ramos, M. C., Durán, B., 2014. Assessment of rainfall erosivity and its spatial and temporal  
720 variabilities: Case study of the Penedès area (NE Spain). *Catena*, 123, 135-147.  
721 <https://doi.org/10.1016/j.catena.2014.07.015>.

722 Renard, K. G., Freimund, J. R., 1994. Using monthly precipitation data to estimate the R-  
723 factor in the revised USLE. *J. Hydrol.* 157(1-4), 287-306. [https://doi.org/10.1016/0022-1694\(94\)90110-4](https://doi.org/10.1016/0022-<br/>724 1694(94)90110-4).

725 Renard, K. G., Foster, G. R., Weesies, G. A., Porter, J. P., 1991. RUSLE: Revised universal  
726 soil loss equation. *J. Soil. Water. Conserv.* 46(1), 30-33.

727 Renard, K.G., Foster, G. R., Weesies, G. A., McCool, D. K., Yoder, D. C., 1997. Predicting  
728 Soil Erosion by Water: A Guide to Conservation Planning with the Revised Universal  
729 Soil Loss Equation. USDA Handbook No. 703, USDA: Washington, DC.

730 Romilly, T. G., Gebremichael, M., 2011. Evaluation of satellite rainfall estimates over

731           Ethiopian river basins. *Hydrol. Earth. Syst. Sc.* 15, 1505-1514. doi:10.5194/hess-15-  
732           1505-2011.

733           Roose, E. J., 1977. Use of the universal soil loss equation to predict erosion in West Africa.  
734           In *Soil erosion: prediction and control*. Soil Conservation Society of America Ankeny,  
735           IA. 21, 60-74.

736           Seaber, P.R., Kapinos, F.P., Knapp, G.L., 1987. *Hydrologic Unit Maps: U.S. Geological*  
737           *Survey Water-Supply Paper*. 2294, 63.

738           Smith, S.V., Renwick, W.H., Buddeemeier, R.W., Crossland, C.J., 2001. Budgets of soil  
739           erosion and deposition for sediments and sedimentary organic carbon across the  
740           conterminous United States. *Glob. Biogeochem. Cycles.* 15, 697-707.  
741           <https://doi.org/10.1029/2000GB001341>.

742           Stanturf, J. A., Goodrick, S. L., Outcalt, K. W., 2007. Disturbance and coastal forests: a  
743           strategic approach to forest management in hurricane impact zones. *Forest Ecol Manag*,  
744           250(1-2), 119-135.

745           Stocking, M.A. and Elwell, H.A., 1973. Prediction of subtropical storm losses from field plot  
746           studies. *Agric. Meteorol.* 12, 193-201. [https://doi.org/10.1016/0002-1571\(73\)90019-8](https://doi.org/10.1016/0002-1571(73)90019-8).

747           Tian, Y., Peters-Lidard, C. D., 2007. Systematic anomalies over inland water bodies in  
748           satellite-based precipitation estimates. *Geophys Res Lett.*, 34(14).

749           Ufoegbune, G. C., Bello, N. J., Ojekunle, Z. O., Orunkoye, A. R., Eruola, A. O., Amori, A.  
750           A., 2011. Rainfall erosivity pattern of Ogun River basin area (Nigeria) using modified  
751           Fournier index. *Eur Water*, 35, 23-29.

752           United States Environmental Protection Agency (EPA)., 2012. Stormwater phase II final rule,  
753           construction rainfall erosivity waiver, Washington, DC, USA, EPA 833-F-00-014.

754           Van Dijk, A. I. J. M., Bruijnzeel, L. A., Rosewell, C. J., 2002. Rainfall intensity-kinetic  
755           energy relationships: a critical literature appraisal. *J. Hydrol.* 261(1-4), 1-23.

756 [https://doi.org/10.1016/S0022-1694\(02\)00020-3](https://doi.org/10.1016/S0022-1694(02)00020-3).

757 Vrieling, A., Sterk, G., de Jong, S. M., 2010. Satellite-based estimation of rainfall erosivity  
758 for Africa. *J. Hydrol.* 395, 235-241. <https://doi.org/10.1016/j.jhydrol.2010.10.035>.

759 Wang, G., Gertner, G., Singh, V., Shinkareva, S., Parysow, P., Anderson, A., 2002. Spatial  
760 and temporal prediction and uncertainty of soil loss using the revised universal soil loss  
761 equation: a case study of the rainfall-runoff erosivity R factor. *Ecol Model.* 153, 143–  
762 155. [https://doi.org/10.1016/S0304-3800\(01\)00507-5](https://doi.org/10.1016/S0304-3800(01)00507-5).

763 Wischmeier, W. H., Smith, D. D., 1958. Rainfall energy and its relationship to soil loss. *Eos,*  
764 *Transactions American Geophysical Union.* 39(2), 285-291.  
765 <https://doi.org/10.1029/TR039i002p00285>.

766 Wischmeier, W.H., Smith, D.D., 1965. Rainfall-Erosion Lossess from Cropland East of the  
767 Rocky Mountains:Guide for selection of practices for soil and water conservation.  
768 USDA Agric. Handbook, No 282, Washington, D.C.

769 Wischmeier, W. H., Smith, D. D., 1978. Predicting rainfall erosion losses-a guide to  
770 conservation planning. Predicting rainfall erosion losses-a guide to conservation  
771 planning.

772 Xie, P., Joyce, R., Wu, S., Yoo, S. H., Yarosh, Y., Sun, F., Lin, R. 2017. Reprocessed, bias-  
773 corrected CMORPH global high-resolution precipitation estimates from 1998. *J.*  
774 *Hydrometeorol.* 18(6), 1617-1641. <https://doi.org/10.1175/JHM-D-16-0168.1>.

775 Yin, S., Xie, Y., Nearing, M. A., Wang, C. 2007. Estimation of rainfall erosivity using 5 to  
776 60-minute fixed-interval rainfall data from China. *Catena* 70(3), 306-312.  
777 <https://doi.org/10.1016/j.catena.2006.10.011>.

778 Zhu, Q., Chen, X., Fan, Q., Jin, H., Li, J., 2011. A new procedure to estimate the rainfall  
779 erosivity factor based on Tropical Rainfall Measuring Mission (TRMM) data. *Sci.*  
780 *China. Tech. Sci.* 54(9), 2437. <https://doi.org/10.1007/s11431-011-4468-z>.

# **Environmental Policies and Political Feasibility: Eco-Labels versus Emission Taxes**

by

Jason M. Walter<sup>†</sup> and Yang-Ming Chang<sup>‡</sup>

April 6, 2020

**Abstract:** This paper examines the economic and political implications of two market-based policies, eco-certifications and emission taxes. We evaluate each policy's effects on the environment, investment in clean technology, and social welfare under imperfect competition. We find that eco-certification reduces total damage to the environment, increases consumer benefits, and is socially desirable. However, polluting firms will never voluntarily accept the socially optimal eco-standard, leading to suboptimal certification programs. Unless the marginal damage to the environment from emissions is sufficiently low and demand is sufficiently large, environmental damage occurring under voluntary eco-certification is higher in comparison to alternative policies. We examine the welfare impacts of each policy to identify social preferences. Using realized market benefits to construct policy preferences, we show conditions under which the socially optimal environmental policy is unlikely to be politically feasible. Our results explain the popularity and suboptimal qualities of eco-certification programs.

**Keywords:** Eco-certification, Emission taxes, Environmental regulations, Green consumers

**JEL codes:** H23, Q5, D62, D43, Q58

The authors declare that they have no conflict of interest.

---

We thank the editor in chief Clevo Wilson and anonymous referees for insightful comments and suggestions, which improved the manuscript considerably. Any remaining errors are ours.

<sup>†</sup>Assistant Professor of Economics, University of Wisconsin-Stout, 721 3<sup>rd</sup> St. E, Menomonie, WI 54751, E-mail: walterja@uwstout.edu; Corresponding author

<sup>‡</sup>Department of Economics, Kansas State University, 319 Waters Hall, Manhattan, Kansas 66506-4001, Tel: (785)532-4573, Fax: (785) 532-6919, E-mail: ymchang@ksu.edu.